

# Seismic observations of glaciogenic ocean waves (micro-tsunamis) on icebergs and ice shelves

Douglas R. MacAYEAL,<sup>1</sup> Emile A. OKAL,<sup>2</sup> Richard C. ASTER,<sup>3</sup> Jeremy N. BASSIS<sup>1</sup>

<sup>1</sup>*Department of Geophysical Sciences, University of Chicago, 5734 South Ellis Avenue, Chicago, Illinois 60637, USA  
E-mail: drm7@midway.uchicago.edu*

<sup>2</sup>*Department of Geological Sciences, Northwestern University, 1850 Campus Drive, Evanston, Illinois 60208-2150, USA*

<sup>3</sup>*Geophysical Research Center and Department of Earth and Environmental Science, New Mexico Institute of Mining and Technology, Socorro, New Mexico 87801, USA*

**ABSTRACT.** Seismometers deployed over a 3 year period on icebergs in the Ross Sea and on the Ross Ice Shelf, Antarctica, reveal that impulsive sources of ocean surface waves are frequent (e.g. ~200 events per year in the Ross Sea) in the ice-shelf and iceberg-covered environment of coastal Antarctica. The 368 events recorded by our field deployment suggest that these impulsive events are generated by glaciological mechanisms, such as (1) small-scale calving and edge wasting of icebergs and ice-shelf fronts, (2) edge-on-edge closing and opening associated with iceberg collisions and (3) possibly the impulsive opening of void space associated with ice-shelf rifting and basal crevasse formation. The observations described here provide a background of glaciogenic ocean-wave phenomena relevant to the Ross Sea and suggest that these phenomena may be exploited in the future (using more purposefully designed observation schemes) to understand iceberg calving and ice-shelf disintegration processes.

## INTRODUCTION

During the austral summers of 2003–06, we operated temporary seismometer arrays on the floating Ross Ice Shelf and on various icebergs (Lazzara and others, 1999) adrift and aground in the Ross Sea, Antarctica (Fig. 1), to detect sources and source mechanisms of iceberg harmonic tremor (IHT) signals observed in the Equatorial Pacific (Talandier and others, 2002, 2006; MacAyeal and others, 2008a) that were apparently emanating from icebergs. An unanticipated by-product of this field effort was the detection of a variety of ocean-surface gravity-wave signals, including tsunamis generated by large earthquakes far from Antarctica (e.g. Okal and MacAyeal, 2006) and sea swell generated by storms located throughout the Pacific and Indian Oceans (Williams and Robinson, 1981; MacAyeal and others, 2006a,b; Cathles and others, in press). In addition to distantly sourced ocean-wave signals, a large number of impulsive, short-duration (1–30 min) wave-arrival events sourced within the Ross Sea were observed. These local signals typically lasted for periods of minutes on seismograms, and had their largest amplitude in the 0.05–0.2 Hz frequency band that is free of distantly sourced weather-related microseism (e.g. Gutenberg, 1947; Williams and Robinson, 1981; Bromirski and Duennebie, 2002; Aster and others, 2008; Cathles and others, in press). As a working hypothesis, we interpret the locally sourced ocean-wave signals in our seismograms as being glaciogenic, i.e. associated with small-scale iceberg calving, iceberg roll-over, iceberg collision, ice-front cliff collapse and rift propagation associated with both icebergs and the ice shelf in the vicinity of our seismometer array.

We refer to these glaciogenic ocean waves as 'micro-tsunamis' because their source mechanisms are impulsive and have short time duration (e.g. iceberg calving, iceberg capsize, steep-ice-surface avalanche, rift opening and iceberg collision, shown schematically in Fig. 2). The term 'micro' is used to signify that the sea-surface (or ice-surface)

displacement amplitude of typical events observed in our study is in the centimeter to micrometer range (i.e.  $\sim 10^{-6}$  of the amplitude of the tragic Indian Ocean tsunami of 26 December 2004 (Synolakis and others, 2005) as recorded in the Ross Sea by Okal and MacAyeal, 2006). We use the term 'micro-tsunami' to emphasize the similarity in physical structure between the relevant waves and those of the great transoceanic tsunamis such as the event of 26 December 2004. Despite the disparity in typical periods between micro-tsunamis studied here and the transoceanic tsunamis generated by earthquakes (i.e. length and time-scales of the two cases can be separated by two orders of magnitude, sufficient to alter the asymptotic regime controlling propagation), both systems consist of physical oscillations exchanging kinetic and gravitational energy in the ocean. Furthermore, a variety of observations during the 2004 Indian Ocean event emphasized the continuity of the tsunami phenomenon from low-frequency and shallow-water propagation towards high-frequency and deep-water propagation, classically associated with ocean swell. In particular, hydrophone observations revealed the continuous dispersion curve of tsunamis between 1 and 10 mHz (Hanson and Bowman, 2005; Okal and others, 2007), and the high-frequency, short-wavelength components of the 2004 Indian Ocean event were found to excite the resonance of harbors in the Indian Ocean several hours after the leading shallow-water waves of the tsunami passed by (Okal and others, 2006). Also, the physics of the wave-generation mechanism described in this study are not intrinsically different from those of tsunamis generated by subaerial and submarine landslides (e.g. in 1999 at Fatu Hiva, Marquesas Islands, South Pacific Ocean (Okal and others, 2002)).

Wave making by tidewater glacier calving is a well-known phenomenon that often excites cruise-ship travelers worldwide. What is less well known is the fact that waves generated by icebergs and calving faces can have near-field amplitudes comparable to life-threatening tsunamis

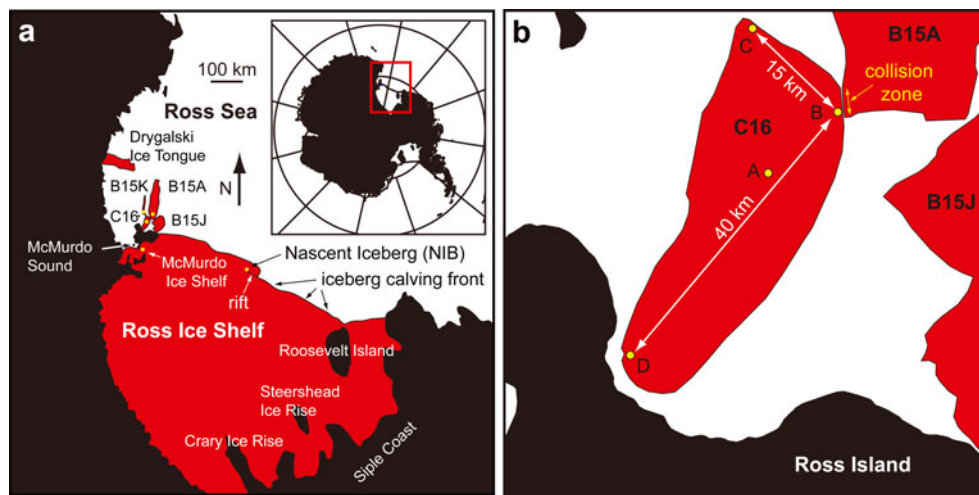


**Fig. 1.** Location map. (a) Seismometer locations for icebergs B15A, B15K, C16 A, McMurdo Ice Shelf and Nascent Iceberg (NIB) denoted by yellow dots. The seismometer location for McMurdo Sound sea ice is denoted by the black dot. Inset: map of Antarctica showing study region. (b) Seismometer array on iceberg C16 during time B15A was colliding with C16's northeastern corner. Seismometer sites A–D indicated by yellow dots.

generated by earthquakes, and can propagate over long distances as small-amplitude events. The dangers of iceberg tsunami genesis are well illustrated by amateur videos documenting this effect at Ilulissat and Umanak, Greenland (<http://www.youtube.com/watch?v=EhmOCAilj2c> and [http://www.youtube.com/watch?v=\\_2NvwlnKVtU](http://www.youtube.com/watch?v=_2NvwlnKVtU)). A particularly compelling amateur video of the research vessel *Nathaniel B. Palmer* attempting to outrun a tsunami generated by iceberg calving in the Antarctic is also available (<http://www.youtube.com/watch?v=tRgTKAWnj4M>).

Glacial wave making in Antarctica is likely to display a wider range of source mechanisms than those in Greenland fjords, including:

1. Edge wasting of the seaward-facing cliffs of ice shelves and icebergs (e.g. by pieces falling into the ocean below, or by submerged pieces rising to the surface from below; Scambos and others, 2008).
2. Inter-iceberg gap closing associated with edge-on-edge collisions between tabular icebergs.
3. Bottom crevasse and rift formation (e.g. Jezek and Bentley, 1983; Bassis and others, 2007).

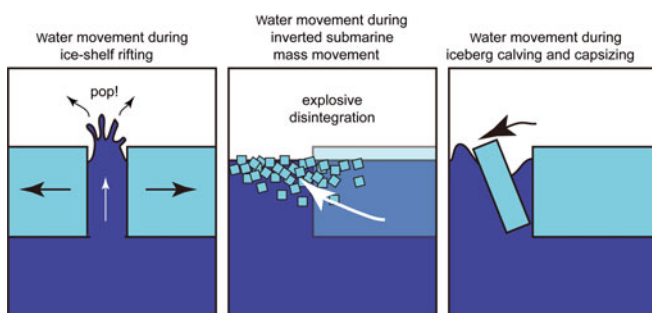


**Fig. 2.** Schematic illustrations of possible glacial tsunamigenic processes (left: rift-opening; middle: ice-shelf disintegration; right: iceberg calving and capsizing).

4. Concertina motions of void space within grounding zones forced by abrupt, stick–slip ice-stream flow (e.g. Bindshadler and others, 2003; Brunt, 2008; Wiens and others, 2008).
5. Submarine landslides at grounding lines where till accumulates in deltas (e.g. Anandkrishnan and others, 2007).
6. Iceberg capsizing (e.g. Bass, 1980; Nye and Potter, 1980; Scambos and others, in press).

For the long length-scale and time-period content of the sea-surface disturbances associated with these mechanisms, the flexural rigidity of floating ice shelves and sea ice does not inhibit wave propagation in the coupled ice-over-water system.

A compelling question associated with glacial wave making is whether it has the potential to inform understanding of iceberg, ice-shelf and sub-ice-shelf processes. With a little imagination, it is possible to speculate that micro-tsunami signals may provide quantitative measures of the rifting processes that dissect ice shelves and that can cause them to disintegrate into collections of hundreds to thousands of small icebergs (e.g. Rott and others, 1996). Glacial earthquakes sourced in Greenland outlet glaciers have provided insight into their acceleration in response to secular increases in surface melting (e.g. Ekström and others, 2003, 2006). The success that seismological techniques have had in monitoring Greenland's ice discharge leads us to inquire whether other types of signals, such as those described here, may be useful for study of Antarctica's iceberg-calving margin.

A starting point for this inquiry is the assessment of the signal environment, i.e. determination of the nature and frequency of wave-making events that may be observed in the coastal Antarctic waters. Our field effort over 2003–06 provides an opportunity for such an assessment. The objective of this communication is to describe the nature and possible source mechanisms of glacial wave making near the seaward margin of the Antarctic ice sheet, and to assess the potential of glaciogenic ocean waves as a means to study icebergs and ice shelves.

## Hydrodynamic preliminaries

Surface gravity waves treated in this study are considered to propagate in both ice-free and ice-covered water. In ice-covered water, the ice cover can consist of broken sea ice, ranging up to several meters thick, to iceberg and ice-shelf cover, with thickness ranging up to several hundred meters. In all cases studied, wave amplitude,  $\eta_0$ , is small compared to water-column thickness (water depth minus ice thickness if ice-covered),  $h$ , which is generally large compared to wavelength,  $\lambda = 2\pi/k$ . Throughout the analysis that follows, wave trains produced from glacial sources will be assumed to be planar, being described by a simple sinusoidal profile of the sea surface (or ice surface, in ice-covered water):

$$\eta(x, t) = \eta_0 \sin(kx - \omega t), \quad (1)$$

where  $\eta(x, t)$  is the free-surface displacement relative to the mean sea level,  $k = 2\pi/\lambda$  is the wavenumber,  $x$  is the direction of propagation,  $\omega = 2\pi/T$  is wave frequency, with  $T$  being wave period, and  $t$  is time. Water motion below the surface of the ice-free ocean, and below the basal surface of any ice cover, is irrotational and restricted to the  $x$ - $z$  plane (Earth rotation effects are assumed to be negligible, provided  $T \ll 2\pi/\Omega$ , where  $\Omega$  is the angular frequency of Earth rotation), where  $z$  is the vertical coordinate, positive upward. These irrotational motions decay with increasing  $z$ . In circumstances where  $\lambda$  is small compared to  $h$  (i.e. the deep-water limit) vertical decay is exponential with an  $e$ -folding scale equal to the horizontal wavelength. In the shallow-water limit, when  $\lambda \gg h$ , horizontal motion in the water associated with the wave is independent of  $z$ . The water is assumed inviscid.

In the absence of flexural effects introduced by ice cover, the equations of hydrodynamics predict that waves of the type described above propagate according to the dispersion formula (Munk and others, 1963):

$$\omega^2 = gk \tanh(kh), \quad (2)$$

where  $g = 9.81 \text{ m s}^{-2}$  is the acceleration due to gravity. Conventional, earthquake and submarine-landslide triggered tsunamis are observed in the low-frequency (or shallow-water) limit for which  $kh \rightarrow 0$  leading to the well-known undispersed relation:

$$\omega^2 = ghk^2, \quad (3)$$

which corresponds to a velocity (both phase,  $C$ , and group,  $U$ ) of

$$C = U = \sqrt{gh}. \quad (4)$$

However, records of the 2004 Indian Ocean tsunami on hydrophone, island seismometers, as well as on our iceberg-deployed seismometers, have detected its dispersion according to Equation (2) throughout the frequency spectrum (Okal, 2005; Okal and MacAyeal, 2006; Okal and others, 2007). In particular, in the high-frequency (or deep-water) limit where  $kh \rightarrow \infty$ , Equation (2) becomes

$$\omega^2 = gk, \quad (5)$$

leading to a phase velocity  $C = \omega/k = g/\omega$  and a group velocity  $U = \partial\omega/\partial k = g/(2\omega) = C/2$  (Munk and others, 1963; Bromirski and Duennebie, 2002). In turn,  $U \approx 1/\omega$  predicts an arrival time linearly dispersed with frequency. This range of frequencies is the traditional domain of sea swell and also of our 'micro-tsunami' observations.

Although of considerable interest, the effects of ice cover on the dispersion and attenuation of waves on the ocean surface (waves in the ice-covered ocean) will not be considered in detail in this study because the limited knowledge of ice-thickness conditions (i.e. thickness maps of icebergs on which seismometers were deployed do not exist) prohibits analysis using results of previous studies (e.g. Williams and Robinson, 1981; Squire and others, 1994, 1995; Squire, 2007). In most cases, our observations suggest that glacial micro-tsunamis are generated by iceberg and ice-shelf fragments that fall into, or otherwise disturb, an ocean that is ice-free or covered by thin, broken sea ice. In this case, propagation of the long-wavelength components of excitation (e.g. with wavelengths  $>100 \text{ m}$ ) is negligibly influenced by sea-ice flexure and attenuation, and analysis of micro-tsunami signals can be performed using the dispersion relation given by Equation (2). In cases where micro-tsunami generation is within the interior of an iceberg or ice shelf, where ice thickness is orders of magnitude larger than for sea ice, ice-flexure effects and attenuation are likely to be significant for even the longest wavelengths generated. We acknowledge this complexity, but refrain from addressing it due to the fact (discussed below) that our observation design did not permit satisfactory determination of micro-tsunami source locations. Without source location, treatment of flexure and attenuation is moot. In spite of our disregard of the flexure and attenuation effects of ice cover, we find that the majority of events witnessed in our observation program were consistent with sources in the open or sea-ice-covered waters of the Ross Sea that allow analysis using the simple dispersion relation given by Equation (2).

One of the important utilities of the dispersion described in Equation (5) is that it allows source-to-receiver distance to be obtained from seismometer observations. Defining the cyclic frequency,  $f = 2\pi/\omega$ , and using the concept of group velocity,  $U = d\omega/dk$ , a relation between  $f$  and wave travel distance,  $\Delta$ , from the source to the receiver is obtained:

$$\frac{df}{dt} = \frac{g}{4\pi\Delta}, \quad (6)$$

where  $t$  in the above context is the observed time at which energy with frequency  $f$  arrives at the receiver. The above formula is used to determine  $\Delta$  from measurements of  $df/dt$  that are obtained on signal spectrograms (described below).

## Field deployment

We deployed seismometers on icebergs in the Ross Sea (C16, B15A, B15K) and on the McMurdo Ice Shelf, the Ross Ice Shelf and on sea ice in McMurdo Sound (Fig. 1). The instruments were Guralp 40T seismometers provided by the Incorporated Research Institutions for Seismology (IRIS) Program for the Array Seismic Studies of the Continental Lithosphere (PASSCAL) instrument pool, and are sensitive to signals in the 0.01–50 Hz range on three axes of motion. Signals were sampled at both 1 and 100 Hz, digitized by Quanterra Q330 equipment and stored in Quanterra Bailers. The seismometers were deployed on ceramic flooring tiles at the bottom of snow pits  $\sim 2 \text{ m}$  deep, that were covered with plywood and snow-block roofs. Solar panels provided power to a 12 V battery system. As discussed by Okal and MacAyeal (2006), these seismometers are able to sense sea-surface motion in the low-frequency range, below  $\sim 0.15 \text{ Hz}$  (corresponding to a period of 6.7 s), and microseisms (e.g. Gutenberg, 1947; Longuet-Higgins, 1950) at frequencies

**Table 1.** Seismometer field deployment start and end dates

Site	Start	End
C16 A–D (4-site array)	October 2003	January 2004
C16 A*	November 2004	November 2005
C16 A	November 2005	– †
McMurdo Ice Shelf	January 2004	October 2004
B15K	November 2004	– ‡
Nascent Iceberg	November 2004	November 2006
McMurdo Sound sea ice	December 2005	November 2006

Note: See table 1 of Okal and MacAyeal (2006) for further details.

\*C16 A's seismometer was incorrectly wired during this period and could not record signals below  $\sim 1$  Hz; thus, data relevant to this study were missing from this time period.

†Currently C16 is adrift off East Antarctica with the seismometer in an unknown state. Data from C16 A were collected up to November 2005.

‡B15K's seismometer was never recovered and its data were never collected.

above this level. Such fidelity to the recording of sea-surface wave conditions is rarely achieved, if at all, in seismometers deployed on grounded ice sheets or on land. The typical frequency content and amplitude of signals recorded by the seismometers is associated with transoceanic propagation of sea swell coming from storms in the distant Pacific and Indian Oceans. These signals are described at length by Cathles and others (in press).

An initial deployment, in October 2003, focused all seismometer placement on iceberg C16, where four sites were operated for a period of  $\sim 3$  months (Fig. 1b). This array provided the opportunity to examine the nature of iceberg motions excited by ocean waves incident on the iceberg's seaward-facing edges. This four-site array was replaced in January 2004 with a single instrument at the C16 center site (site A in Fig. 1b), and was maintained during the 2004 and 2005 field seasons. In January 2006, C16 drifted away from the range of logistical operations, and the iceberg and seismometer (with data collected since early November, 2005) are currently located off the coast of East Antarctica.

From January 2004 onward, single-seismometer stations were deployed on icebergs C16, B15A, B15K, the McMurdo Ice Shelf (near the US and New Zealand scientific bases), on landfast, multi-year sea ice in McMurdo Sound, and on the Ross Ice Shelf (at a site called 'Nascent Iceberg' where a large-scale tabular iceberg is expected to calve in the next decade; Fig. 1a). Table 1 summarizes the periods of deployment and data collection for these stations. Generally speaking, the instruments operated throughout the period solar charging was possible, and did not operate during the period from roughly the end of May to mid-October of each year of the field program. All data are in the process of being archived at the IRIS Data Management Center.

## GLACIOGENIC OCEAN-WAVE EVENT CATALOGUE

The glaciogenic-wave signals catalogued from our data are short-duration packets (ranging in duration from less than  $\sim 5$  min to more than  $\sim 3$  hours) possessing energy in the sub-0.15 Hz frequency range where wavelengths ( $> 70$  m) are sufficiently large to avoid the attenuation associated with flexural effects in sea-ice-covered water. Examples

of catalogued signals, displayed as both vertical channel seismograms and spectrograms, are displayed in Figure 3. Histograms of event frequency as a function of time-of-year for three locations (C16, McMurdo Ice Shelf and Nascent Iceberg) are displayed in Figure 4. Periods where instruments were 'asleep' from lack of solar charging are masked in gray, and yellow masking denotes periods where background noise associated with sea swell from weather systems in the Pacific, Southern and Indian Oceans saturates the spectrograms in the sub-0.15 Hz range and makes detection of glaciogenic waves impossible.

The catalogue consists of 368 events from probable glacial sources in the Ross Sea, and was assembled from the 2003–06 field campaign (see Table 1) using the following identification method. Spectrograms of the 1 s sample rate vertical motion channel (referred to as LHZ; unprocessed instrument output in units of 'counts', which are proportional to vertical ground velocity) of each seismometer's output were constructed for each day, and linear streaks (signifying dispersion) of relatively high-signal spectral density were identified by visual inspection (i.e. linear energy swaths on the spectrograms were distinguished from noise by noting the impulsivity, signal duration and dispersion associated with local wave sources). Event distance (determined from dispersion; see below) and timing were recorded as part of the catalogue, and some events were noted as having certain peculiar features, such as being significantly higher in amplitude than other events.

In Figure 3, signals are most prominently displayed as upper-right-verging linear swaths of high signal density in the spectrograms. The upper-right tilt signifies arrival of a dispersed wave train (with low frequency arriving before high frequency) from a temporally constrained, possibly impulsive, source. Spectrograms in Figure 3 present the signal spectral-energy density (in dB of  $\log_{10}$  of  $\text{counts}^2 \text{Hz}^{-1}$ ) created using the Matlab™ 'spectrogram()' command with data-windowing parameters chosen to obtain a good visual representation of the wave arrival (the data window parameter was 600 s and the window overlap parameter was 500 s, as described in Matlab documentation; see <http://Mathworks.com>). For high-amplitude events in the catalogue, the arrival of waves can be seen in the associated seismograms shown in Figure 3, which plot raw LHZ instrument output as a function of time. The majority of events were of low amplitude, however, and could only be detected above background noise (mostly sea swell) by noting their dispersion features visible in spectrograms.

## Background noise

For events to be added to the catalogue, their signal had to be distinguishable from background noise in the 0.01–0.15 Hz band and had to have frequency dispersion implying a local ( $< 500$  km) source, so as to rule out signals originating from storms and other events beyond the glacial environment of Antarctica. Waves with frequencies higher than  $\sim 0.15$  Hz were typically not observed due to attenuation by sea ice surrounding the icebergs or ice shelf, and by reflection at the cliff-like seaward-facing edges of the iceberg or ice shelf. Waves with frequencies lower than  $\sim 0.05$  Hz were typically not observed due to the constant bobbing motion of the icebergs and ice shelf at this frequency. Floating ice of thickness  $h_i$  and density  $\rho_i$  bobs at

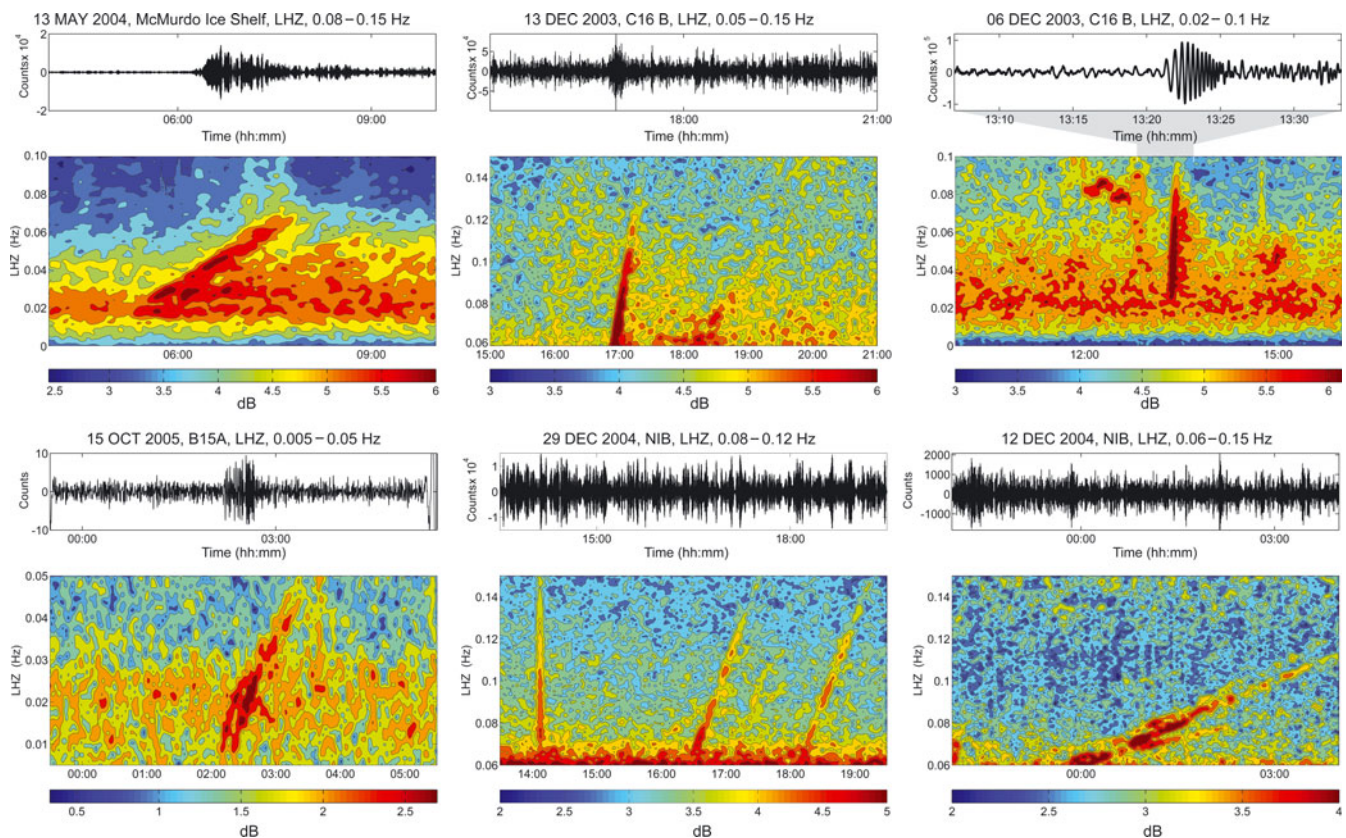


**Fig. 3.** Examples of six glaciogenic ocean-wave events (micro-tsunamis) recorded during the 3 year seismometer deployment on icebergs and ice shelf in the Ross Sea. For each example a section seismogram of vertical channel (LHZ) seismometer output (units of counts, proportional to ground velocity) is displayed above a signal spectrogram of the event (dB of  $\log_{10}$  of counts<sup>2</sup> Hz<sup>-1</sup>; color bars at bottom). Typical spectrogram patterns indicate linear frequency dispersion patterns (i.e.  $df/dt \approx \text{constant}$ , where  $f$  is signal frequency and  $t$  is time) consistent with surface-gravity wave dispersion associated with deep-water limits and null elastic-flexure effects. The slopes of the linear dispersion patterns are used to estimate distances each event's wave train traveled as a deep-water wave (i.e. through water not covered by thick iceberg or ice shelf). The event in the upper-right panel displays a close-up of the seismogram, because the waveform is particularly impulsive and well distinguished from noise.

a period  $T$  given by (Schwerdtfeger, 1980)

$$T = 2\pi \sqrt{\frac{\rho_i h_i}{\rho_w g}}, \quad (7)$$

where  $\rho_w$  is the density of sea water and  $g = 9.81 \text{ m s}^{-2}$ . For  $h_i \sim 250 \text{ m}$ , the approximate thickness of the Ross Ice Shelf at the Nascent Iceberg site, this period is  $\sim 30 \text{ s}$ , giving a frequency of maximum noise  $\sim 0.03 \text{ Hz}$ . For  $h_i \sim 75 \text{ m}$ , the approximate average thickness of iceberg C16 and of the McMurdo Ice Shelf, this period is  $\sim 16 \text{ s}$ , giving a frequency of maximum noise  $\sim 0.06 \text{ Hz}$ . Background noise recorded by the seismometers on iceberg C16, and on the McMurdo and Ross Ice Shelves, conforms to the frequency band of bobbing motions (pitching and rolling motions are also possible, at slightly higher frequency (Okal and MacAyeal, 2006)) and are probably excited by passing meteorological conditions and by ocean swell propagating into the Antarctic from afar (e.g. Williams and Robinson, 1981; MacAyeal and others, 2006b). The band of noise in the 0.01–0.06 Hz range is well displayed by the spectrograms of all example events shown in Figure 5a.

### Glacial source identification criteria

Once candidate events for the catalogue are differentiated from noise in the above manner, their likelihood of being

generated by glacial mechanisms is determined using the following criteria:

1. Their duration within the seismogram or spectrogram record, including the effect of dispersion, is short (i.e. less than  $\sim 3$  hours). This distinguishes the glaciogenic ocean-wave signals from those that are generated by meteorological events (e.g. lasting days, as described by Cathles and others, in press).
2. They often display quasi-periodicity (e.g. arriving at the same time of day over a number of days) at timescales associated with the dominant diurnal tide of the Ross Sea. This implies a source mechanism that is sensitive to ocean tide. Ocean tide is seen to be an important driver of iceberg motion (MacAyeal and others, 2008b) and modulates ice-shelf and ice-stream flow (Bindschadler and others, 2003; Brunt, 2008; Wiens and others, 2008).
3. Frequency dispersion implies a source within the local glaciated environment of the Ross Sea (e.g. distances inferred from dispersion range from  $\sim 1$  to  $\sim 500 \text{ km}$ ). This range is consistent with sources along the calving fronts of the ice shelf, the edges of the icebergs, outlet glaciers along the coastlines and rifts and other features within the ice shelf, both proximal to the ice front and proximal to the grounding lines.

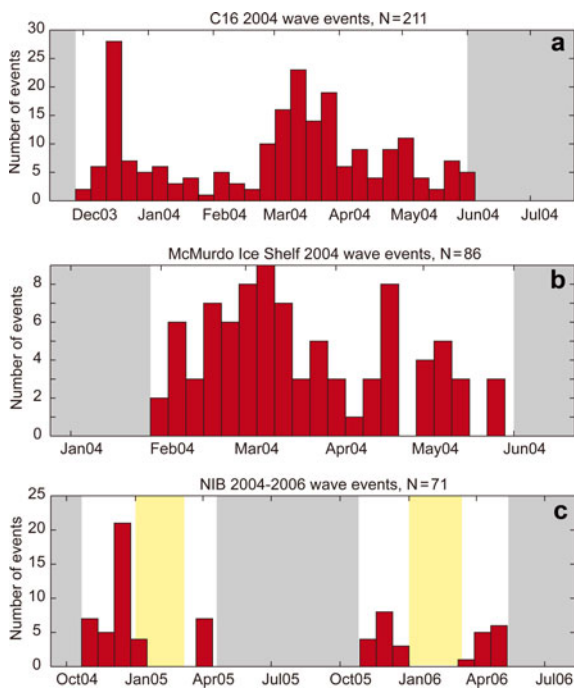


**Fig. 4.** Histograms of event timing for events observed at (a) C16 A, (b) McMurdo Ice Shelf and (c) Nascent Iceberg (NIB). Times when seismometers were asleep due to lack of photovoltaic battery charging are masked in gray. Times when micro-tsunami events could not be distinguished because of excessive background noise in the 0.05–0.15 Hz frequency range are masked in yellow.

- Efforts were made to rule out other impulsive arrivals such as those associated with teleseismic earthquake signals and local iceberg harmonic tremor (IHT) signals.

The above criteria for discriminating glaciogenic sources from others are admittedly ad hoc, and room exists for occasional misidentification of signals that neither have glacial origin nor propagate as ocean surface waves. We were particularly attentive to two classes of signals that could be prone to misidentification. The first of these two classes concerns signals arriving from teleseismic earthquake sources: typically a weak *P*-wave arrival followed by a high-amplitude dispersed surface- or Rayleigh-wave arrival. Teleseismic earthquake signals were received on the icebergs and the Ross Ice Shelf, despite the fact that they are disconnected from the solid Earth by an intervening sea-water layer. The large length scale of teleseismic waves means that the water and ice layers move in concert with the seabed (Okal and MacAyeal, 2006). An example of a teleseismic earthquake signal is shown in Figure 5a, and results from a magnitude 6.7 earthquake that occurred in the Pacific, northwest of North America, at a distance of  $\sim 131^\circ$ . The characteristic upper-right verging 'hook' of the solid-Earth surface-wave arrival in the spectrogram is used to identify the event as a teleseismic earthquake signal. Note, in particular, that its dispersion is not linear in the 0.05–0.07 Hz range. Also seen in Figure 5a is a faint *P*-wave arrival as a broad, undispersed vertical band of barely discernible energy in the spectrogram  $\sim 45$  min prior to the hook-like

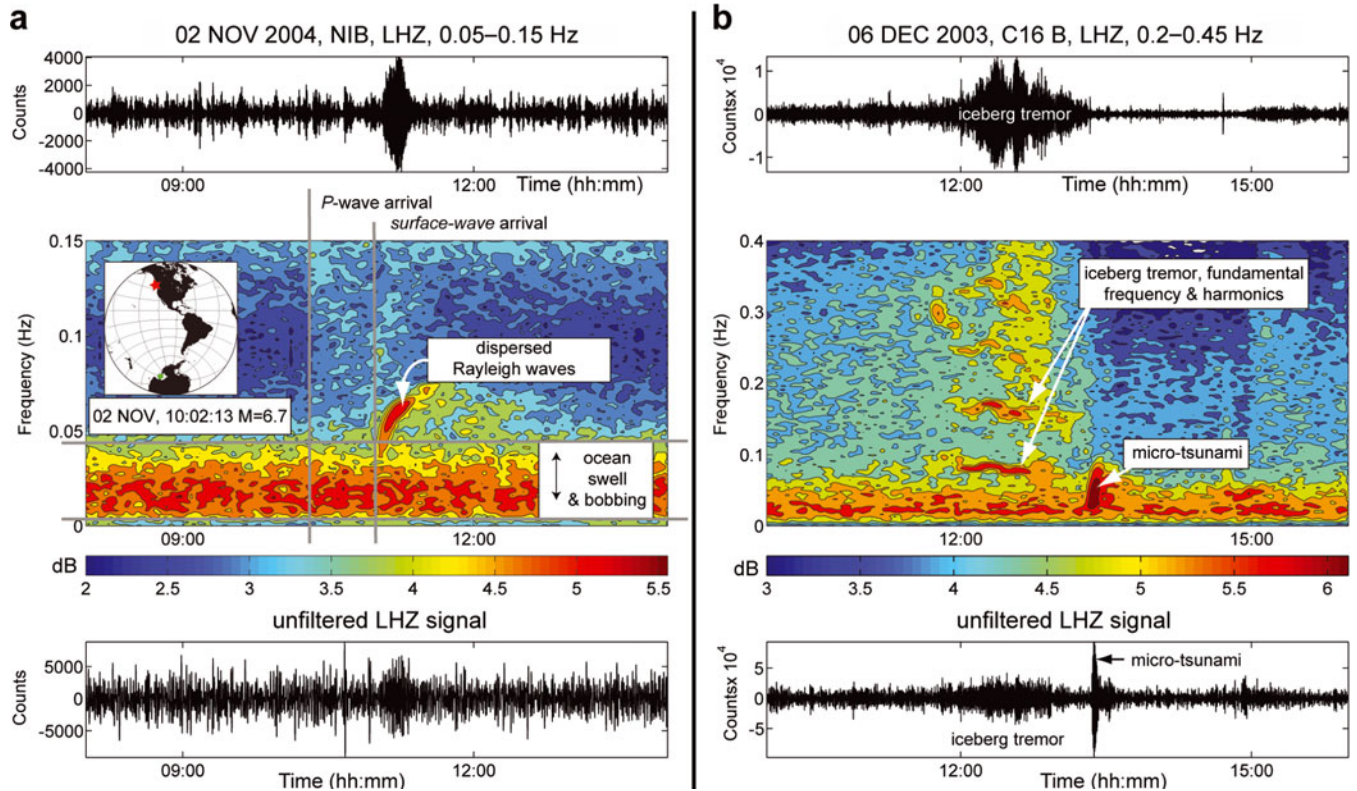


**Fig. 5.** Background noise and other seismic signals to be excluded from the event catalogue. (a) Earthquake arrival recorded at Nascent Iceberg (NIB); top panel: vertical ground motion (LHZ) seismogram filtered (four-stage Butterworth filter) to 0.05–0.15 Hz frequency band; middle panel: spectrogram of signal (dB of  $\log_{10}$  of counts $^2$ Hz $^{-1}$ ; color bar at bottom); bottom panel: unfiltered vertical (LHZ) seismogram. Inset: map showing source and receiver for  $M=6.7$  earthquake on Pacific coast of North America. Ocean noise due to ice-shelf buoyancy oscillations (bobbing) indicated by bright signal strength in spectrogram between two horizontal gray lines. *P*-wave and surface-wave (Rayleigh wave) arrival of the earthquake indicated by vertical gray lines. (b) Iceberg tremor and micro-tsunami recorded on C16, site B (Fig. 1).

surface-wave arrival. (*S*-wave arrivals were typically not observed at our seismometer sites, due to their low expected amplitude exacerbated by losses in the conversion of shear motions to vertical motions at the sea bottom.) Our heuristic signal-identification technique involved looking for signs of *P*-wave arrival and the tight, hook-like curvature of the spectrogram energy swath signifying the arrival of Rayleigh waves.

The second class of signal excluded from the catalogue arises from IHT described by MacAyeal and others (2008a). IHT is generated by stick-slip motion along the edge-on-edge contact between two tabular icebergs that are slowly sliding past each other. Typically there are thousands of discrete stick-slip events over a period of hours, and their inter-event time spacing (typically 0.1–10 s) leads to a striated, or 'chevron', pattern in signal spectrograms. An example of IHT in its low-frequency range that overlaps with the <0.15 Hz signals of glaciogenic wave-making events is shown in Figure 5b. To discriminate between ocean wave trains associated with glaciogenic sources and short bursts of IHT, we looked for (1) the classic pattern of integer-multiple harmonics that exist at frequencies higher than the fundamental sub-0.15 Hz vibration of the IHT and (2) the possible presence of high-frequency (above ~5 Hz) hydro-acoustic signals also generated by stick-slip motions at the edges of colliding icebergs and observed as seismo-acoustic phases at our stations (MacAyeal and others, 2008a).

### Ice-flexure effects

An initially perplexing feature of the ocean-wave signals in our catalogue is that they appear very simple, showing little immediately recognizable effect of the flexural rigidity of the ice cover on which the seismometers were deployed. To illustrate an event where flexural rigidity effects are important, we show the signal generated on the sea ice of McMurdo Sound resulting from the landing of a 100 000 kg aircraft on a 5 m thick sea-ice runway overlying water (>100 m deep) near McMurdo Station (Fig. 6). The flexural-gravity-wave signal from the aircraft landing was observed at a seismometer located ~1800 m from the point where the aircraft touched down and ~1350 m from the point where the maximum reverse thrust was applied on the aircraft engines. The seismometer was located ~100 m from the side of the runway, and so was in the expected maximum radiation pattern for flexural-gravity waves of a load moving at high speed across the runway surface.

The seismograms and spectrogram associated with the aircraft landing are shown in Figure 6. The top seismogram displays the 1 s sample rate LHZ signal filtered into the 0.01–0.5 Hz band. At face value, this signal would appear to be a compact packet of surface gravity waves generated by some impulsive event in the ocean surrounding the seismometer site. What distinguishes it as a packet of flexural gravity waves involving the elastic flexure mechanics of the sea ice is the fact that short wavelengths (high frequencies) arrive at the seismometer before long wavelengths (low frequencies). This dispersion pattern is the reverse of the pattern of dispersion for surface waves traveling on deep water in the absence of a flexurally rigid ice layer. This pattern is also opposite to the normal dispersion characteristics for seismic surface waves. Ice-flexural dispersion is seen in the bottom seismogram of Figure 6, which shows the 0.01 s sample rate vertical ground-motion seismogram signal. In the spectrogram, the arrival of the wave packet generated by

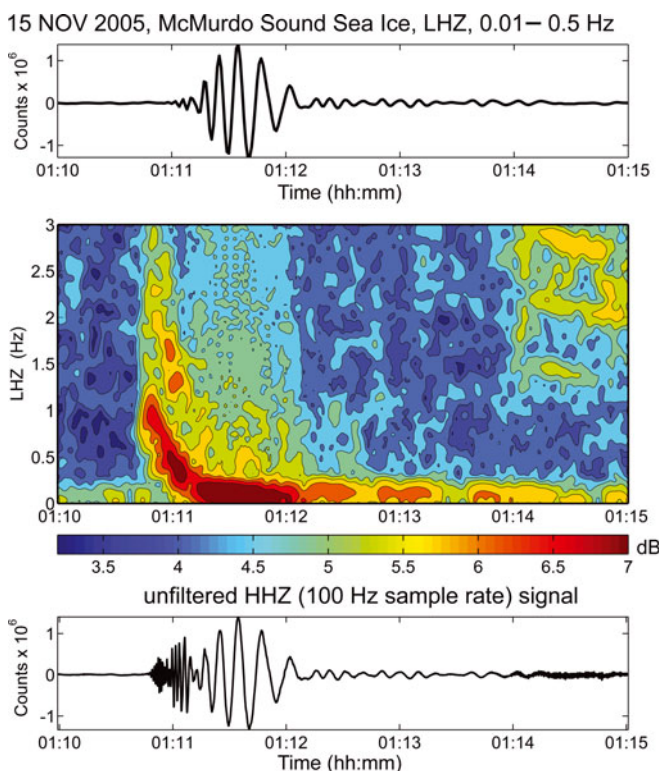


**Fig. 6.** Flexural-gravity wave on a sea-ice covered ocean surface recorded by a seismometer on landfast, multi-year sea ice (~5 m thick) in McMurdo Sound (Fig. 1) generated by the landing of a large cargo aircraft (Boeing C17). Top panel: Seismogram of vertical channel (LHZ) filtered to 0.05–0.15 Hz frequency band (four-stage Butterworth filter); middle panel: LHZ spectrogram displaying right-upward concave pattern characteristic of flexural-gravity wave propagation (dB of  $\log_{10}$  of counts<sup>2</sup>Hz<sup>-1</sup>; color bar at bottom); bottom panel: unfiltered HHZ (100 Hz sample rate vertical channel) seismogram of same event. Initial aircraft wheel-on-runway touchdown and secondary reverse thrust application are apparent in both the spectrogram and HHZ seismogram.

the aircraft landing shows a characteristic upper-left verging curvature indicative of the effects of elastic flexure on short-wavelength waves. First arrivals are of the highest-frequency energy; later arrivals involve the low-frequency waves that are not as strongly influenced by elastic flexure of the ice. Two other features in the spectrogram of the aircraft landing are interesting: the initial touchdown of the aircraft on the ice surface appears to be followed by a second series of waves generated by the application of reverse thrust on its jet engines (the energy >1.5 Hz that appears after 01:11) and there is a high-frequency tremor appearing after 01:14 of unknown origin.

By far the majority of surface-wave phenomena observed on the icebergs and the Ross Ice Shelf lacked the tell-tale signs of elastic-flexure dispersion described above. An example of this is given in Figure 7, showing C16 when four seismometers were operating. The signal is observed at all stations at roughly the same time (exact arrival times could not be determined because the signals were too noisy) with identical frequency dispersion, i.e. identical  $df/dt$ , where  $f$  is the cyclic frequency and  $t$  is the time of observation. Site B (Fig. 1b) displays the largest signal in both the LHZ spectrogram (shown) and seismogram (not shown), with the brightest spectral-energy swath showing the distinctive linearity signifying a source-to-receiver distance of ~15 km

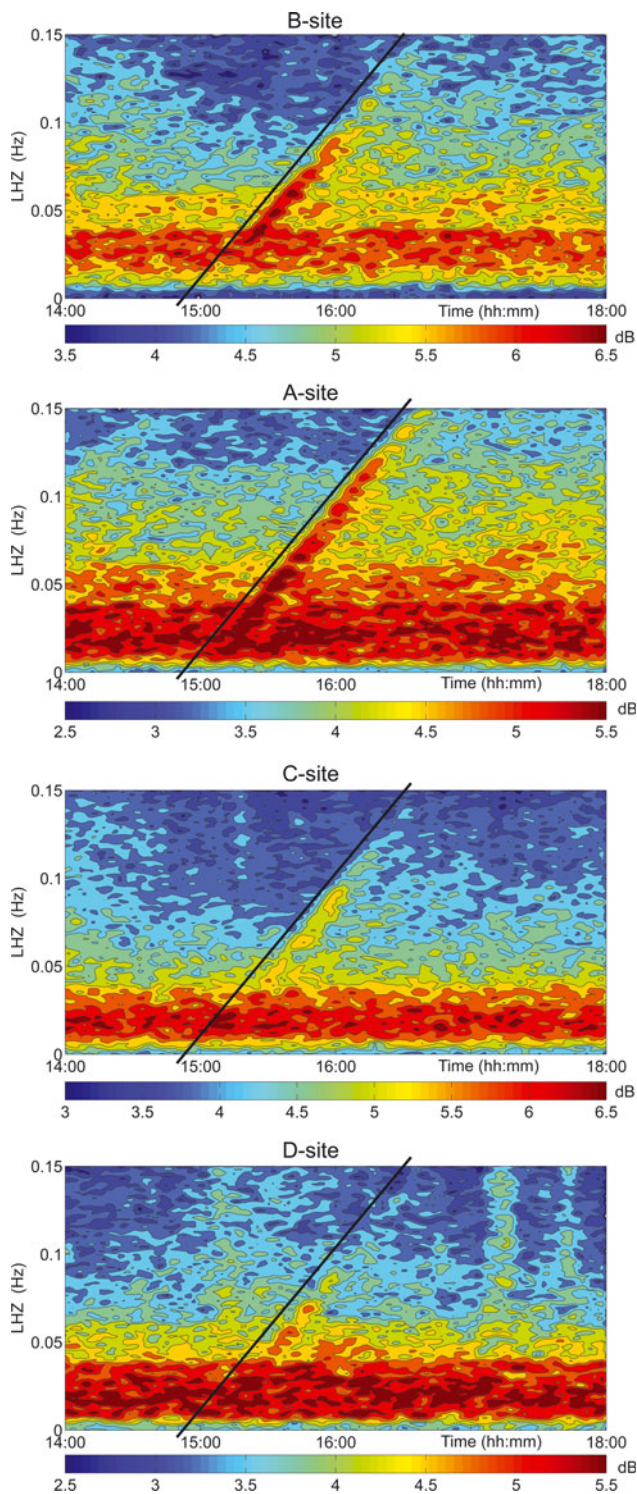


**Fig. 7.** LHZ spectrograms of micro-tsunami arrival (16 December 2003 at approximately 16:00) at four seismometer stations on C16 (Fig. 1b) ( $\text{dB of } \log_{10} \text{ of counts}^2 \text{ Hz}^{-1}$ ; color bars at bottom). Except for signal amplitude and noise level, the signatures of the micro-tsunami represented by the sloping signal density swaths in the spectrograms are virtually identical at all four sites. The slope (black line) at site A is identical to those of the three other sites (black lines), and indicates that signal dispersion along paths that traverse the iceberg is negligible. This suggests that wave dispersion is primarily a function of the open-water leg of wave-train travel to the iceberg, and that the signal, once it reaches the iceberg, is transmitted to sites within the iceberg through a combination of flexural and rigid-body motions of the iceberg. The lack of significant dispersion within the iceberg, and the lack of easily identified arrival times associated with the emergent signals, made it impossible to determine micro-tsunami source locations from the C16 seismometer array.

(as discussed below). Comparing the spectrograms from the other three sites (A, C and D) with that of site B reveals that the slope of the signal is the same for all sites, implying an identical source-to-receiver distance of  $\sim 15$  km, despite the intervening distance between site B and the other sites. This uniformity of  $df/dt$  implies that travel of the wave train across the iceberg from the station closest to the source to the station most distant from the source produces little discernible dispersion associated with flexure effects. (A thorough analysis of how such effects would be manifest is left for future theoretical treatments.)

The absence of the characteristic signature of flexural-gravity-wave dispersion in spectrograms of events in our catalogue (e.g. Figs 3 and 7) initially surprised us, and this inspired a detailed analysis of several of the strongest events recorded by the four-station seismometer array on C16 to determine why. Investigation of the iceberg-surface (ground) motion revealed that the initial vibration of the iceberg excited by wave trains incident somewhere on its seaward-facing edge was almost immediately transmitted (e.g. within several wave periods) to all other parts of the iceberg. This is consistent with the expected high propagation velocity of flexural-gravity waves (e.g. Holdsworth and Glynn, 1978; Goodman and others, 1980; Williams and Robinson, 1981; Kristensen and others, 1982) for ice in the 50–150 m thickness range measured on C16 at the four seismic stations, using a hand-held pulse radar. The extreme rapidity of flexural-gravity-wave transmission resulted in short travel times between the site of initial excitation (i.e. a seaward-facing edge onto which an ocean wave train is incident) and distant sites elsewhere on the iceberg. Dispersion by flexural effects within the iceberg leg of wave propagation was thus insignificant (owing to the short travel times). Dispersion effects associated with surface-gravity-wave propagation in ice-free (or thinly covered) ocean conditions evident from a given wave train's propagation across an open-water leg leading from the source to the iceberg's seaward-facing edge was preserved without distortion, and recorded at all points on the iceberg uniformly. All seismometers on the iceberg record motion at the same frequency, because flexural effects transmit frequency changes observed at the initial point of excitation across the iceberg with a timescale shorter than that of frequency change associated with the incident wave energy.

To illustrate the above explanation for the lack of flexural-gravity-wave dispersion patterns in catalogue event seismograms, a schematic diagram of elastic-flexural effects on the iceberg is shown in Figure 8. An initial glacial wave-making event, such as the collapse of a seaward-facing ice cliff (Fig. 8, right), generates an impulsive wave that subsequently propagates a distance through open water (or through water covered by sea ice of insufficient thickness to introduce elastic-flexure effects). During the open-water propagation leg, the initially impulsive wave front is dispersed into a wave train led by long-wavelength/low-frequency energy and trailed by short-wavelength/high-frequency energy. Eventually, the dispersed wave train impinges on the edge of the iceberg (Fig. 8, on the right of the tabular iceberg). Relative to the timescale necessary to transmit the edge excitation across the length of the iceberg, the edge excitation of the impinging wave appears monochromatic, i.e. the time evolution of the frequency of the impinging waves determined by dispersion in the open-ocean environment is slow compared to the transmission time of waves at a given frequency

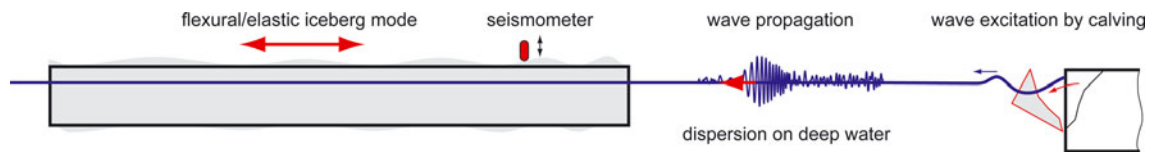


**Fig. 8.** Schematic diagram showing (1) micro-tsunami generation by small-scale edge wasting of seaward-facing ice cliff, (2) micro-tsunami dispersion on deep water during travel across ice-free ocean surface, (3) excitation of vibration at the seaward-facing ice cliff of an iceberg's edge or ice shelf's ice front and (4) subsequent fast propagation as flexural-gravity wave through iceberg/ice-shelf interior to various receiving stations. The waveform depicted in flight between the source and the receiver is adopted from the observed micro-tsunami signal shown in the upper-right panels of Figure 3.

across the iceberg by elastic-flexure effects. Seismometers at locations spread across the iceberg thus sense the frequency information of the impinging wave, but not the change in this frequency information associated with the short-timescale dispersion effects of flexural rigidity.

### Flexural-gravity resonance modes of iceberg

The considerations in the preceding subsection explain the observed fact that flexural effects are generally absent from the glaciogenic wave-making events recorded in our

catalogue. The same considerations can be used to suggest that the icebergs (and likely the Ross Ice Shelf as well) are subject to flexural oscillations excited by the waves that impinge on them (e.g. Goodman and others, 1980; Wadhams and others, 1983; Squire and others, 1994; Squire, 2007). To investigate this possibility, we again examined the four-station seismometer motions on iceberg C16.

As shown in Figure 9, the kinematics of horizontal and vertical ice-surface movement on C16 is complex. The horizontal polarization of iceberg-surface (ground) motion

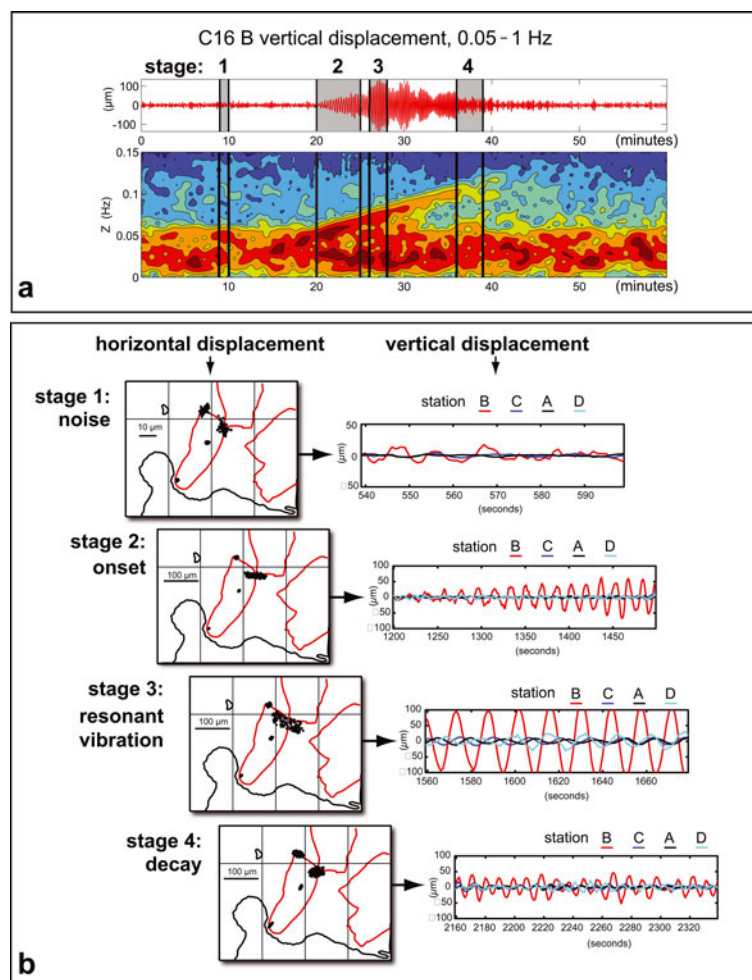


**Fig. 9.** Iceberg (ground) displacements during the arrival of a micro-tsunami recorded on 16 December 2003. (a) A seismogram (upper graph) and a spectrogram (lower graph) of C16 B site's vertical displacement during a 60 min period of micro-tsunami arrival. The seismogram signal was filtered to the 0.05–0.15 Hz frequency band using a four-stage Butterworth filter. The vertical displacement seismogram is in units of dB of  $\log_{10}$  of  $m^2 s^2 Hz^{-1}$ ; red color denotes high signal strength. The vertical displacement seismogram (upper graph) is divided into four segments to display stages of signal evolution (labeled 1–4). Stage 1 represents pre-event noise; stage 2 represents event onset; stage 3 represents event development as a flexural/elastic mode of iceberg vibration (resonance); stage 4 represents event decay. (b) Maps of exaggerated horizontal position (left panels) and graphs of vertical motion (right panels) for each of the four stages of evolution designated in (a).

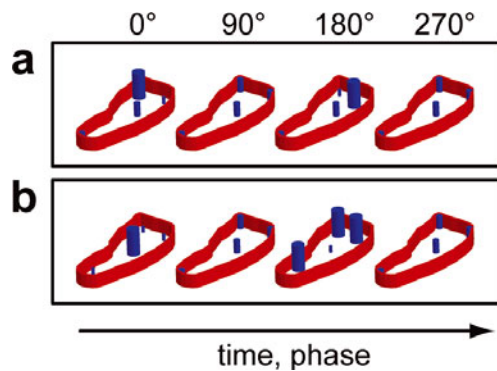


**Fig. 10.** Two vertical modes of iceberg vibration determined from vertical displacements of the seismometers. Station displacements are shown schematically as cylinders (height of cylinder denotes position relative to undisturbed location) at various phases of the oscillation. (a) Iceberg vibration involving 'see-saw' of the northern end (top in figure) of the iceberg, with relatively little motion in other parts of the iceberg. (b) 'Trampoline' mode of iceberg vibration where the center of the iceberg goes up and down, out of phase with the edges of the iceberg.

and relative phasing between the sites changes as the frequency of an arriving event changes according to its spectrogram. As the maps of horizontal ice-surface motion recorded by the seismometers suggest (Fig. 9), the horizontal polarity of seismometer motion at each of the four sites (represented by the elliptical patterns of point locations superimposed on the map using an exaggerated horizontal scale) changes as the frequency of the event evolves (as shown on the spectrogram of Fig. 9). The vertical motions at each of the four sites also change, progressing from uncorrelated 'noisy' motions prior to the event's arrival, to phase-coordinated sinusoidal vibrations as the frequency of the arriving wave train passes through specific ranges (e.g.  $\sim 0.065$  Hz for the map labeled 3 in Fig. 9 and its associated sub-seismogram). Gentle undulations of the amplitude envelope of the vertical ice-surface motion seismogram recorded at site B, on the northeast corner of C16, suggest that different modes of iceberg vibration are being excited in sequence.

The vertical and horizontal motions observed at the seismometer sites during four sub-intervals of the evolution of a single micro-tsunami arrival are displayed in Figure 9b. These motions suggest that there are four distinct stages in the response of the iceberg to the excitation induced by incoming waves in the ocean. Stages 2–4 suggest the progressive excitation of successive eigenmodes of the iceberg's flexure, such as those modes illustrated in Figures 10 and 11. We relegate to future study the question of the identification and further analysis of such modes, which will likely require a considerable quantitative effort to compare our observations with simulations of iceberg/ocean modes. In Figure 10, the two most distinguishable vertical modes of vibration are depicted (we do not know how these modes relate to the spectrum of other eigenmodes (e.g. whether they are most grave or not)). The lowest-frequency vibration is a 'see-saw' motion of the two corners defining the northern end of C16, with relatively little movement in the rest of the iceberg. The next-highest-frequency mode consists of a 'trampoline' motion involving oscillation between the center of the iceberg and its two

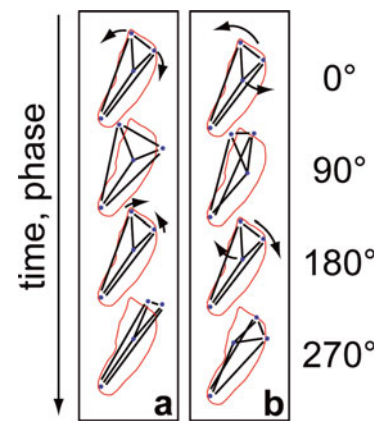


**Fig. 11.** Two horizontal modes of iceberg vibration determined from horizontal displacements of the seismometers. Station displacements are shown schematically as stick figures at various phases of the oscillation (dots denote station location; sticks are line segments connecting stations). (a) Iceberg vibration involving dilatation of the northern end (top in figure) of the iceberg, with relatively little motion in other parts of the iceberg. (b) Iceberg vibration involving twisting of the northern end of the iceberg relative to the center of the iceberg.

ends. The northern end of C16 was originally part of the Ross Ice Shelf closest to the shear zone where the ice shelf flows past the eastern end of Ross Island (Fig. 1), defining the western end of the ice-shelf extent. Airborne radar surveys of C16 conducted in the early and mid-1970s, when it was still part of the Ross Ice Shelf (Bentley and others, 1979), suggest that this end of the iceberg (constituting the northern end during the seismometer observation campaign) was thin, with ice thicknesses ranging below 100 m. This is confirmed by point radar measurements at sites B and C when the seismometers were deployed, giving thicknesses of  $53 \pm 5$  and  $40 \pm 5$  m, respectively. It is likely that this thin area of the iceberg would vibrate with the slowest-frequency see-saw mode due to its reduced flexural rigidity (which depends on the cube of ice thickness). The higher-frequency vibration of the trampoline mode may be explained by the greater thickness, and hence flexural rigidity, of the rest of the iceberg relative to the area of the northern end. Ice-thickness measurements at sites A and D are  $145 \pm 20$  and  $150 \pm 20$  m, respectively; thus, motions involving the central, elastically stiffer, part of the iceberg should have higher frequency.

Horizontal modes of oscillation are depicted in Figure 11, where the two most distinguishable horizontal modes of vibration visible in animations made using seismometer horizontal displacements are (1) a stretching mode of the line segment formed by the two corners defining the northern end of C16 (sites B and C) where the iceberg is relatively thin and (2) a torsional mode involving twisting oscillation of the northern end of the iceberg relative to its center. Consideration of the ice-thickness and flexural-rigidity variations on the iceberg again suggests that the stretching mode should be lower-frequency than the torsional mode, which involves torsion of the thicker 'waist' of the iceberg near site A.

## DETERMINATION OF EVENT DISTANCE

Unfortunately, we could not use standard algorithms of triangulation to locate the source of our events, because

of unexpected flaws in the geometry of the seismometer arrays, and because often only single seismometer stations were operating at any one time. Except for the approximately 3 month period (October 2003–January 2004) when a four-seismometer array was operated on C16, the observation scheme consisted of either (1) a single seismometer operating alone (e.g. the November 2004–November 2005 operation of Nascent Iceberg's seismometer, while C16 A's seismometer had an electronic problem that limited sensitivity to the  $>1$  Hz frequency range) or (2) a pair of seismometers operating at distances too great to observe the same events (e.g. the November 2005–November 2006 period when seismometers operated at Nascent Iceberg and on the McMurdo Sound sea ice) or (3) a pair of seismometers separated by complex intervening island geometry (e.g. the January 2004–May 2004 period when seismometers were operating at both C16 A and on the McMurdo Ice Shelf, but were separated by Ross Island).

Even during the  $\sim 3$  month period when a four-seismometer array operated on C16, source location was still frustrated by the effects of signal conversion from surface-gravity waves to flexural-gravity waves along the iceberg's seaward-facing edges. In essence, the iceberg's flexural rigidity was sufficiently large to homogenize the seismic signals at the four stations (so that they recorded essentially the same signal, as if located at the same spot on the iceberg). The vibrational modes of the iceberg, when excited by wave trains in the ocean surrounding the iceberg, were emergent signals that could not be precisely timed or located. In essence, the four-station seismic array on C16 could do nothing more than determine (1) the distance (from deep-water dispersion effects) the wave train traveled in deep, ice-free water (or sea-ice-covered water) and (2) the time of wave arrival on a seaward-facing iceberg edge of undetermined location. (Efforts to inquire more deeply into analysis techniques that may possibly overcome these difficulties are left for future study.)

For the events in our catalogue,  $df/dt$  is linear (in all but one or two cases, as demonstrated in, e.g., the examples of Fig. 3) and is thus compatible with Equation (6). This confirms that the working hypothesis, that the deep-water limit applies to the events of the catalogue, is sufficient for further analysis. This further suggests that wave events of the catalogue spend significant time traveling in open water that is significantly deeper (e.g. by a factor of 2) than the wavelength. For waves propagating on deep water with periods between 7 and 20 s (e.g. as in our catalogue), the wavelength is in the range 70–625 m. The depth of water below the icebergs near Ross Island and near the ice-front region of the Ross Ice Shelf where our seismometers were deployed ranges from 500 to 1000 m (Davey, 2004).

Event distance ( $\Delta$ ) statistics, computed from  $df/dt$  on spectrograms using Equation (6), are summarized for three receiver sites (C16 A, McMurdo Ice Shelf and Nascent Iceberg) by the histograms and maps shown in Figures 12 and 13. (The observations from the McMurdo Sound sea ice displayed too few events to be statistically of interest, due to the higher noise levels in the sea ice that obscured glaciogenic wave events.) Event-distance distribution is unimodal for C16 and the McMurdo Ice Shelf, with peak frequencies of  $\sim 15$  and  $\sim 100$  km, respectively, and is bimodal for Nascent Iceberg with peaks near  $\sim 50$  and  $\sim 400$  km. Plots of circles with radii equal to individual event distances also show the bimodality of Nascent Iceberg

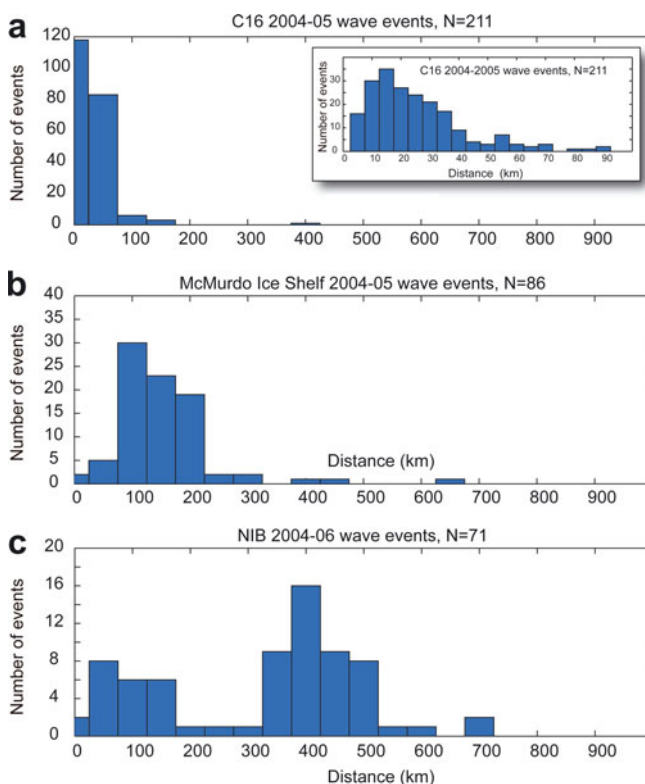


**Fig. 12.** Source-to-receiver distance ( $\Delta$ ) histograms for events received at various seismometer sites through the various observation periods. Distance is calculated using Equation (6), and represents the distance traveled by the waves over open-water portions of the Ross Sea where deep-water dispersion characteristics apply. Additional distance is traveled between the point where the wave energy is received at the edge of the iceberg or ice shelf on which the receiver (seismometer station) is located; however, this additional distance cannot be determined from the data because dispersion effects associated with propagation in ice-covered water (where ice is significantly thicker than seasonal sea ice) are unknown. The statistics shown above provide some measure of micro-tsunami source location, but they should be interpreted only as a lower bound on source-to-receiver distance.

relative to C16 and the McMurdo Ice Shelf (Fig. 13). Due to the imprecise nature of the interpretation of these distances (i.e. they reflect merely the distance traveled in ice-free water), we can only speculate as to the meaning of the event-distance statistics displayed in Figures 12 and 13. For the sites displaying unimodal distributions of event distance (C16 and McMurdo Ice Shelf), we suggest that the sources of the events are predominantly restricted to the edges of the icebergs on the north side of Ross Island. The bimodal distribution of Nascent Iceberg also suggests that the edges of the icebergs are contributing to a majority of the signals, as the circles with larger radii in Figure 13 roughly encompass the icebergs north of Ross Island. These larger-radii circles, corresponding to the long-distance mode of the event-distance distribution for Nascent Iceberg, also encompass the areas of disturbed ice shelf (e.g. where surface and basal crevasses are formed and where there are rifts and other voids) downstream of various ice rises along the Siple Coast (e.g. Cray Ice Rise, Steershead Ice Rise and Roosevelt Island). It is thus interesting to note that intra-ice-shelf sources (not comprising the seaward-facing boundary of the ice shelf) are potentially consistent with the observations conducted

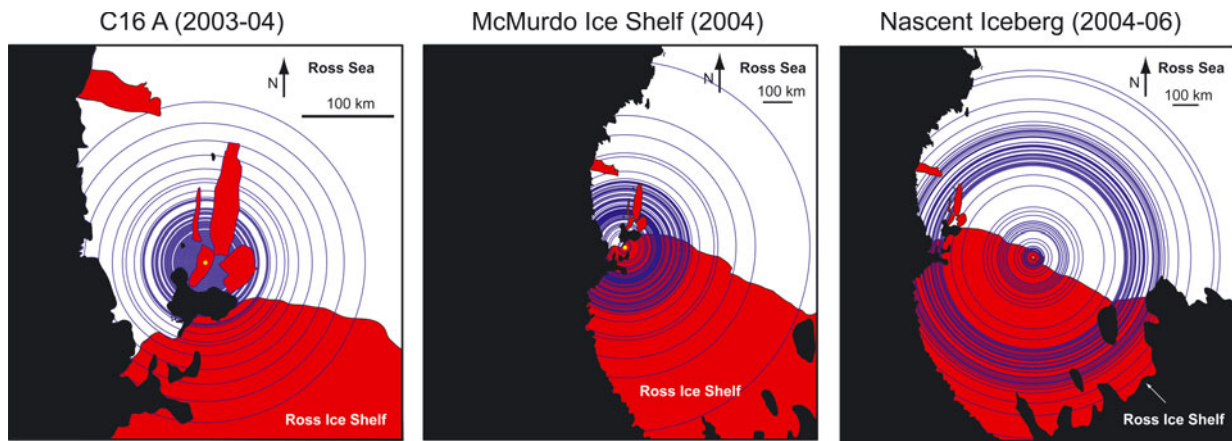


**Fig. 13.** Maps of micro-tsunami source loci associated with events recorded on iceberg C16 site A (left), McMurdo Ice Shelf (middle) and Nascent Iceberg (right). Source loci are small circles mapped around the various receiver sites (seismometer sites) with radii given by the  $\Delta$ 's determined from Equation (6). While insufficient to unambiguously locate event sources (due to the stations not operating at the same time or not recording the same events simultaneously), the small circles in each of the three panels are consistent with sources in the collision zones between the icebergs north of Ross Island, with sources around the edges of the icebergs and with sources along the calving front of the Ross Ice Shelf or in the interior edges of ice-shelf rifts.

so far; however, events sourced in these areas would have to contend with propagation primarily through ice-covered water, so dispersion effects associated with the deep-water limit of ice-free water would not be expected to strictly apply, as has been the simplifying assumption of the present study.

The smaller-radii circles centered on Nascent Iceberg (Fig. 13) correspond to the short-distance mode of the event-distance distribution. Sources on these radii may be associated with (1) the large ice-shelf rift expected to be the future detachment rift of the Nascent Iceberg (this rift is the extension of a larger rift extending from Roosevelt Island to the approximate location of Nascent Iceberg that allowed the calving of B15 in March 2000), (2) edge wasting of the front of the Ross Ice Shelf and (3) possible rift widening (and rift-edge infall) in the ice-shelf rifting zones that extend downstream (relative to ice-shelf flow) of Cray Ice Rise (location shown in Fig. 1a).

### Event periodicity and source location

The wave-train travel-distance information derived above supports the notion that the majority of the glaciogenic sources are associated with icebergs that were located north of Ross Island during the field campaign. Collisions between these icebergs driven by the gyrations of B15A and B15J associated with ocean tides were noted as a major kinematic feature of these icebergs (MacAyeal and others, 2008b). It is thus reasonable to inquire whether events of the catalogue occur on a quasi-periodic, diurnal basis given the strong dominance of the diurnal tide in the southwestern Ross Sea (MacAyeal, 1984; Robertson and others, 1998; Padman and others, 2003). Examination of events observed on C16 reveals that, indeed, a great many tend to occur at the same time of day for several days in a row. These periodic events are also often associated with IHT episodes which are generated by stick-slip cycles produced by tangential motions in edge-on-edge contact zones between two icebergs (MacAyeal and others, 2008a). These associations imply that a majority of the events are associated with iceberg collisions that are paced by the ocean tide.

### DISCUSSION

The main result of our study is the initial phenomenological description of a type of microseismic signal heretofore unrecorded in the large-scale ice-shelf environment of Antarctica. We attribute this result to our good fortune to be among the first to deploy sensitive broadband seismometers in new glaciological settings; in our case, on floating icebergs and ice shelves. This suggests that additional efforts to conduct seismic observations in novel glaciological settings may continue to provide new and informative types of signals useful in the study of glaciological processes.

### Micro-tsunamis as informative signals

The most significant conclusion drawn from our observations is the realization that micro-tsunami signals generated by floating portions of the Antarctic ice sheet are commonplace and readily observed. This result invites speculation about whether micro-tsunami signals might inform study of iceberg-calving and ice-shelf-disintegration processes; and about whether glaciogenic tsunamis (close to source, where amplitude can be in the meters range) may themselves play a mechanical role in stimulating iceberg calving and ice-shelf disintegration. A disappointing aspect of our field campaign was that the design of our seismometer array was inadequate to pin down the source locations and focal mechanisms of micro-tsunamis. Our failure in this regard does not, however, rule out the possibility of gathering this important information if the seismometer array design is judiciously improved.

Assuming that this technical improvement is feasible, we suggest that observations of micro-tsunamis on ice shelves prone to 'Larsen-style' disintegration may help in understanding the dynamics of explosive ice-shelf disintegration. Recent study of the explosive collapse of parts of the Wilkins Ice Shelf in February and May 2008 (Braun and others, 2008; Braun and Humbert, 2009; Scambos and others, in press) suggests that the disintegration was due to a calving and mass-movement process concentrated on the calving edge rather than due to a process that simultaneously affected large areas of the ice-shelf interior. Satellite imagery (Scambos and others, 2009) suggests that the disintegration was an edge-wasting process that initially produced many small,

uncapsized ice-shelf fragments of various sizes, and that a large population of these fragments (notably with width smaller than thickness) subsequently capsized and fragmented into small, irregularly shaped pieces. To further differentiate between 'edge wasting' and 'ice-shelf interior' processes that play in ice-shelf disintegration, a study of micro-tsunamis generated by iceberg calving, capsize and fragmentation would be warranted. By deploying seismometers on a disintegrating ice shelf (e.g. in the rear of a disintegrating ice shelf which may be expected to survive the disintegration intact), the locus of micro-tsunami signal sources could potentially distinguish between edge and interior source mechanisms.

### Glaciogenic tsunamis as a forcing mechanism

The extreme rapidity of the break-up of portions of the Wilkins Ice Shelf in February 2008 (Braun and others, 2008; Braun and Humbert, 2009) suggests that the requisite calving, capsizing and break-up of ice-shelf fragments is a self-stimulating, chain-reaction-type process that requires mechanical processes capable of acting over large distances with short, sub-diurnal timescales (e.g. following the ideas of R.A. Massom and others (unpublished information)). This suggestion is exemplified best by the comparison of MODIS (moderate-resolution imaging spectroradiometer) imagery between 28 and 29 February 2008, when  $\sim 150 \text{ km}^2$  of unfragmented ice-shelf area converted into a densely packed mass of small icebergs that expanded seaward from the original edge of the ice shelf at a rate of  $\sim 0.3 \text{ m s}^{-1}$  ([http://nsidc.org/news/press/20080325\\_Wilkins.html](http://nsidc.org/news/press/20080325_Wilkins.html)). Simple, rough consideration of the energetics associated with ice and sea-water movement during the fragmentation and capsize processes indicates that the gravitational potential energy,  $\Delta E$ , released by the ice-shelf disintegration process is:

$$\Delta E = \frac{1}{2} \rho_i g \left( 1 - \frac{\rho_i}{\rho_w} \right) AH \Delta H, \quad (8)$$

where  $H$  is the original thickness of ice shelf,  $H - \Delta H$  is the thickness of idealized 'ice rubble' occupying the ocean surface after disintegration,  $A$  is the surface area of ice shelf involved in disintegration, and  $\rho_i$  and  $\rho_w$  are the densities of ice and sea water, respectively. We note that the above expression is positive definite. Evaluating the above formula for conditions associated with the disintegration of the Wilkins Ice Shelf in February 2008, where initial ice-shelf thickness is  $\sim 180 \text{ m}$ , the final ice-rubble thickness is  $\sim 50 \text{ m}$ , and where a  $10 \text{ km}$  by  $35 \text{ km}$  area of the original ice shelf is involved, gives:

$$\Delta E \approx 4 \times 10^{15} \text{ J}. \quad (9)$$

If all this energy is converted into kinetic energy,  $T = 1/2 \rho_i A H V^2$ , the velocity,  $V$ , of the seaward-moving mass of ice rubble (typically seen as a blue bubble in the wake of an outer edge of uncapsized ice-shelf fragment icebergs in the MODIS imagery) following disintegration will be  $\sim 11.7 \text{ m s}^{-1}$ . This velocity is far above that implied by the expansion rate of the ice-rubble mass in the MODIS imagery of 28 and 29 February 2008 (i.e.  $\sim 0.3 \text{ m s}^{-1}$ ). The implication is that a large fraction of potential energy released by the disintegration is radiated hydrodynamically as traveling tsunamis. These tsunamis may subsequently interact with unbroken, uncapsized icebergs and the remaining intact, undisintegrated ice shelf to help sustain the disintegration process. Break-up of one small segment of the ice shelf could produce tsunamis that cause other parts of the ice shelf that

have been preconditioned by environmental and climate-change effects (e.g. surface melting (Scambos and others, in press)) to disintegrate. This idea is admittedly speculative, but it serves to illustrate how further seismological observations of glaciogenic micro-tsunami signals may inform understanding of the ice-shelf disintegration process.

### CONCLUSION

While it is premature to suggest that glaciogenic micro-tsunamis will be as useful as, for example, long-period glaciogenic earthquakes in studying ice-sheet response to environmental change (e.g. Ekström and others, 2006), we believe that it is prudent to continue to assess their potential in this regard. Many phenomena, such as the disintegration of ice shelves along the Antarctic Peninsula, involve potential disturbances to the equilibrium of the local sea surface that can radiate micro-tsunami signals. These signals should thus form the focus of further study to develop both a phenomenological understanding of their source and propagation characteristics and to develop temporal statistics necessary to detect changes in ice-shelf stability.

### ACKNOWLEDGEMENTS

Financial and logistical support was provided by the US National Science Foundation (NSF) under the following grants: OPP-0229546, OPP-0538414, OPP-0229492, OPP-0230028, ANT07-39769 and OPP-0229305. Various Raytheon Polar Services Co. personnel and crew of the PHI and Kenn Borek aircraft services provided invaluable assistance in seismometer deployment and recovery. T. Parker and N. Barstow of IRIS PASSCAL trained the field teams and T. Parker participated in the initial field deployment on iceberg C16. Field assistants included J. Thom, M. Okal, A. Bliss, K. Brunt, M. Cathles and various members of the McMurdo Station community. Instruments were provided by the PASSCAL facility of the Incorporated Research Institutions for Seismology (IRIS) through the PASSCAL Instrument Center at the New Mexico Institute of Mining and Technology. IRIS facilities are supported by Cooperative Agreement NSF EAR-000430 and the US Department of Energy National Nuclear Security Administration. We thank P. Bromirski, S. Anandakrishnan and various attendees of the 2008 IRIS Workshop for valuable discussions at initial stages of this research. We thank T. Scambos for his service as the scientific editor, and reviewers R. Coleman and M. Fahnestock who provided considerable help during the revision of the manuscript.

### REFERENCES

- Anandakrishnan, S., G.A. Catania, R.B. Alley and H.J. Horgan. 2007. Discovery of till deposition at the grounding line of Whillans Ice Stream. *Science*, **315**(5820), 1835–1838.
- Aster, R.C., D.E. McNamara and P.D. Bromirski. 2008. Multidecadal climate-induced variability in microseisms. *Seismol. Res. Lett.*, **79**(2), 194–202.
- Bass, D.W. 1980. Stability of icebergs. *Ann. Glaciol.*, **1**, 43–47.
- Bassis, J.N., H.A. Fricker and J.B. Minster. 2007. Seismicity and deformation associated with ice-shelf rift propagation. *J. Glaciol.*, **53**(183), 523–536.
- Bentley, C.R., J.W. Clough, K.C. Jezek and S. Shabtaie. 1979. Ice-thickness patterns and the dynamics of the Ross Ice Shelf, Antarctica. *J. Glaciol.*, **24**(90), 287–294.

- Bindschadler, R.A., M.A. King, R.B. Alley, S. Anandkrishnan and L. Padman. 2003. Tidally controlled stick-slip discharge of a West Antarctic ice stream. *Science*, **301**(5636), 1087–1089.
- Braun, M. and A. Humbert. 2009. Recent retreat of Wilkins Ice Shelf reveals new insights in ice shelf break-up mechanisms. *Geosci. Remote Sens. Lett.*, **46**(2), 263–267.
- Braun, M., A. Humbert and A. Moll. 2008. Changes of Wilkins Ice Shelf over the past 15 years and inferences on its stability. *Cryos. Discuss.*, **2**(3), 341–382.
- Bromirski, P.D. and F.K. Duennebieer. 2002. The near-coastal microseism spectrum: spatial and temporal wave climate relationships. *J. Geophys. Res.*, **107**(B8), 2166. (10.1029/2001JB000265.)
- Brunt, K.M. 2008. Tidal motion of the Ross Ice Shelf and its interaction with the Siple Coast Ice Streams, Antarctica. (PhD thesis, University of Chicago.)
- Cathles, L.M., E.A. Okal and D.R. MacAyeal. In press. Seismic observations of sea swell on the floating Ross Ice Shelf, Antarctica. *J. Geophys. Res.*
- Davey, F.J. 2004. *Ross Sea bathymetry, 1:2 000 000, version 1.0*. Lower Hutt, Institute of Geological Nuclear Sciences. (Map no. 16.)
- Ekström, G., M. Nettles and G.A. Abers. 2003. Glacial earthquakes. *Science*, **302**(5645), 622–624.
- Ekström, G., M. Nettles and V.C. Tsai. 2006. Seasonality and increasing frequency of Greenland glacial earthquakes. *Science*, **311**(5768), 1756–1758.
- Goodman, D.J., P. Wadhams and V.A. Squire. 1980. The flexural response of a tabular ice island to ocean swell. *Ann. Glaciol.*, **1**, 23–27.
- Gutenberg, B. 1947. Microseisms and weather forecasting. *J. Meteorol.*, **2**, 21–28.
- Hanson, J.A. and J.R. Bowman. 2005. Dispersive and reflected tsunami signals from the 2004 Indian Ocean tsunami observed on hydrophones and seismic stations. *Geophys. Res. Lett.*, **32**(17), L17608. (10.1029/2005GL023783.)
- Holdsworth, G. and J.E. Glynn. 1978. Iceberg calving from floating glaciers by a vibrating mechanism. *Nature*, **274**(5670), 464–466.
- Jezeq, K.C. and C.R. Bentley. 1983. Field studies of bottom crevasses in the Ross Ice Shelf, Antarctica. *J. Glaciol.*, **29**(101), 118–126.
- Kristensen, M., V.A. Squire and S.C. Moore. 1982. Tabular icebergs in ocean waves. *Nature*, **297**(5868), 669–671.
- Lazzara, M.A., K.C. Jezeq, T.A. Scambos, D.R. MacAyeal and C.J. van der Veen. 1999. On the recent calving of icebergs from the Ross Ice Shelf. *Polar Geogr.*, **23**(3), 201–212.
- Longuet-Higgins, M.S. 1950. A theory of the origin of microseisms. *Philos. Trans. R. Soc. London, Ser. A*, **243**, 1–35.
- MacAyeal, D.R. 1984. Numerical simulations of the Ross Sea tides. *J. Geophys. Res.*, **89**(C1), 607–615.
- MacAyeal, D.R., E.A. Okal and R.C. Aster. 2006a. Ambient seismic signals observed in iceberg-filled waters of the Ross Sea, Antarctica. [Abstr. S41A-1317.] *Eos*, **87**(52).
- MacAyeal, D.R. and 13 others. 2006b. Transoceanic wave propagation links iceberg calving margins of Antarctica with storms in tropics and Northern Hemisphere. *Geophys. Res. Lett.*, **33**(17), L17502. (10.1029/2006GL027235.)
- MacAyeal, D.R., E.A. Okal, R.C. Aster and J.N. Bassis. 2008a. Seismic and hydroacoustic tremor generated by colliding icebergs. *J. Geophys. Res.*, **113**(F3), F03011. (10.1029/2008JF001005.)
- MacAyeal, D.R., M.H. Okal, J.E. Thom, K.M. Brunt, Y.-J. Kim and A.K. Bliss. 2008b. Tabular iceberg collisions within the coastal regime. *J. Glaciol.*, **54**(185), 371–386.
- Munk, W.H., G.R. Miller, F.E. Snodgrass and N.F. Barber. 1963. Directional recording of swell from distant storms. *Philos. Trans. R. Soc. London, Ser. A*, **255**(1062), 505–584.
- Nye, J.F. and J.R. Potter. 1980. The use of catastrophe theory to analyse the stability and toppling of icebergs. *Ann. Glaciol.*, **1**, 49–54.
- Okal, E.A. 2005. Seismic records of the 2004 Sumatra and other tsunamis: a quantitative study. *Pure Appl. Geophys.*, **164**(2–3), 325–253.
- Okal, E.A., G.J. Fryer, J.C. Borrero and C. Ruscher. 2002. The landslide and local tsunami of 13 September 1999 on Fatu Hiva (Marquesas Islands; French Polynesia). *Bull. Soc. Géol. France*, **173**(4), 359–367.
- Okal, E.A., H.M. Fritz, R. Raveloson, G. Joelson, P. Pancosková and G. Rambolamanana. 2006. Madagascar field survey after the December 2004 Indian Ocean tsunami. *Earthquake Spectra*, **22**(S3), S263–S283.
- Okal, E.A. and D.R. MacAyeal. 2006. Seismic recording on drifting icebergs: catching seismic waves, tsunamis and storms from Sumatra and elsewhere. *Seismol. Res. Lett.*, **77**(6), 659–671.
- Okal, E.A., J. Talandier and D. Reymond. 2007. Quantification of hydrophone records of the 2004 Sumatra tsunami. *Pure Appl. Geophys.*, **164**(2–3), 309–323.
- Okal, M.H. 2005. Characteristics of iceberg collisions. (MS thesis, University of Chicago.)
- Padman, L., S. Erofeeva and I. Joughin. 2003. Tides of the Ross Sea and Ross Ice Shelf cavity. *Antarct. Sci.*, **15**(1), 31–40.
- Robertson, R., L. Padman and G.D. Egbert. 1998. Tides in the Weddell Sea. In Jacobs, S.S. and R.F. Weiss, eds. *Ocean, ice and atmosphere: interactions at the Antarctic continental margin*. Washington, DC, American Geophysical Union, 341–369. (Antarctic Research Series 75.)
- Rott, H., P. Skvarca and T. Nagler. 1996. Rapid collapse of northern Larsen Ice Shelf, Antarctica. *Science*, **271**(5250), 788–792.
- Scambos, T. and 7 others. 2008. Calving and ice shelf break-up processes investigated by proxy: Antarctic tabular iceberg evolution during northward drift. *J. Glaciol.*, **54**(187), 579–591.
- Scambos, T. and 7 others. In press. Ice shelf disintegration by plate bending and hydro-fracture: satellite observations and model results of the 2008 Wilkins Ice Shelf break-ups. *Earth Planet. Sci. Lett.*
- Schwerdtfeger, P. 1980. Iceberg oscillations and ocean waves. *Ann. Glaciol.*, **1**, 63–65.
- Squire, V.A. 2007. Of ocean waves and sea-ice revisited. *Cold Reg. Sci. Technol.*, **49**(2), 110–133.
- Squire, V.A., W.H. Robinson, M. Meylan and T.G. Haskell. 1994. Observations of flexural waves on the Erebus Ice Tongue, McMurdo Sound, Antarctica, and nearby sea ice. *J. Glaciol.*, **40**(135), 377–385.
- Squire, V.A., J.P. Dugan, P. Wadhams, P.J. Rottier and A.K. Liu. 1995. Of ocean waves and sea ice. *Annu. Rev. Fluid Mech.*, **27**, 115–168.
- Synolakis, C., E. Okal and E. Bernard. 2005. The megatsunami of December 26, 2004. *The Bridge*, **35**(2), 26–35.
- Talandier, J., O. Hyvernaud, E.A. Okal and P.-F. Piserchia. 2002. Long-range detection of hydroacoustic signals from large icebergs in the Ross Sea, Antarctica. *Earth Planet. Sci. Lett.*, **203**(1), 519–534.
- Talandier, J., O. Hyvernaud, D. Reymond and E.A. Okal. 2006. Hydroacoustic signals generated by parked and drifting icebergs in the Southern Indian and Pacific Oceans. *Geophys. J. Int.*, **165**(3), 817–834.
- Wadhams, P., M. Kristensen and O. Orheim. 1983. The response of Antarctic icebergs to ocean waves. *J. Geophys. Res.*, **88**(C10), 6053–6065.
- Wiens, D.A., S. Anandkrishnan, J.P. Wineberry and M.A. King. 2008. Simultaneous teleseismic and geodetic observations of the stick-slip motion of an Antarctic ice stream. *Nature*, **453**(7196), 770–774.
- Williams, R.T. and E.S. Robinson. 1981. Flexural waves in the Ross Ice Shelf. *J. Geophys. Res.*, **86**(C7), 6643–6648.